Energy Advances

ROYAL SOCIETY OF CHEMISTRY

PAPER

View Article Online
View Journal | View Issue

Cite this: *Energy Adv.*, 2024, 3, 2965

Solvent assisted shape dependent $MAPbI_3$/polyfluorene heterostructures with a larger surface area for improved photocatalytic H_2 evolution†

Tamal Pal,[a] Soumalya Bhowmik,[b] Arvin Sain Tanwar,[a] Ameer Suhail,[b] Nageswara Rao Peela,[bc] Chivukula V. Sastri*[a] and Parameswar Krishnan Iyer*[ab]

Received 17th July 2024,
Accepted 21st October 2024

DOI: 10.1039/d4ya00457d

rsc.li/energy-advances

Although lead based $MAPbI_3$ has been used as a material for photocatalytic hydrogen evolution, conventionally synthesized $MAPbI_3$ in HI solution suffers from very low HER activity with a hydrogen evolution rate of 30 μmol h^{-1} g^{-1}. Several efforts have been made to boost the HER performance by tagging a co-catalyst. But no such significant approach was developed to improve the HER activity of pristine $MAPbI_3$. In this work, the shape and morphology of $MAPbI_3$ have been modified by a simple solvent change route. This led to substantial transformation in shape and morphology affecting various facets of photocatalytic and photoelectrochemical performance. DMF assisted pristine $MAPbI_3$ exhibited an HER activity of 830 μmol h^{-1} g^{-1}, almost 28-fold better than that of typical HI based $MAPbI_3$. This work highlights how solvent transition from HI to DMF can influence the shape and surface morphologies which impact the photocatalytic and photoelectrochemical performances of pristine $MAPbI_3$. To further enhance the HER activity of DMF assisted $MAPbI_3$, the as-synthesized polyfluorene co-catalyst was integrated on the $MAPbI_3$ surface. Under optimized conditions, the hydrogen evolution of $MAPbI_3$/polyfluorene composites can reach up to 6200 μmol h^{-1} g^{-1}.

Introduction

The generation of solar driven green hydrogen (H_2) fuel has been put forward as a potential solution to address the ever-increasing crisis of global energy demand and environmental pollution concerns.[1–3] The utilization of diversified semiconductor photocatalysts for photocatalytic H_2 evolution has garnered significant attention as a sustainable and environmentally-friendly method for converting solar energy into H_2.[4–6] When considering the utilization of solar energy, an efficient photocatalyst should have an appropriate bandgap and conduction band minima in order to effectively capture a wide range of sunlight wavelengths and transfer the photogenerated charges to form H_2 fuel. Hybrid organic–inorganic perovskites ($MAPbI_3$) possess a remarkable absorption coefficient (10^4–10^5 cm^{-1}) with optical bandgap (1.5 eV). These properties enable them to effectively absorb visible light within a wavelength range of approximately 400 nm to 800 nm.[7,8] Furthermore, $MAPbI_3$ (MAPI) demonstrates exceptional electronic characteristics, including ambipolar charge transport and a long charge diffusion length (approximately 25 μm in MAPI single crystals). As a result, it has significantly enhanced the power conversion efficiency of $MAPbI_3$ based solar cells, achieving over 20%.[9–12] $MAPbI_3$ possesses these attractive characteristics that allow it to emerge as a promising contender for the photocatalytic HER. However, its inherent instability in aqueous solutions presents a formidable obstacle when it comes to its application in photocatalysis. Recently, Park and co-workers have successfully tackled this challenge by skillfully establishing a delicate equilibrium between the solvation and crystallization of $MAPbI_3$ in a saturated aqueous HI solution. As a result, they were able to achieve photocatalytic H_2 evolution through HI splitting. This breakthrough opens up new avenues for harnessing the potential of $MAPbI_3$ in photocatalytic processes.[13] However, when compared to traditional semiconductors, the observed rate of hydrogen evolution reaction (HER) of $MAPbI_3$ in an aqueous solution of HI is relatively low. This is likely due to the significant recombination of

[a] *Department of Chemistry, Indian Institute of Technology Guwahati, Guwahati 781039, Assam, India. E-mail: pki@iitg.ac.in*
[b] *Centre for Nanotechnology, Indian Institute of Technology Guwahati, Guwahati 781039, Assam, India*
[c] *Department of Chemical Engineering, Indian Institute of Technology Guwahati, Guwahati 781039, Assam, India*

† Electronic supplementary information (ESI) available: Synthesis of materials, photochemical and photoelectrochemical measurements. See DOI: https://doi.org/10.1039/d4ya00457d

photogenerated charges within the microcrystals of $MAPbI_3$. Recent studies have demonstrated that the incorporation of electron transporters, such as Pt, TiO_2, MoS_2, CoP, carbonized polymer dots, black P, and NiCoB combined with the $MAPbI_3$ photocatalyst, can enhance the efficiency of charge transportation by quickly extracting the photogenerated electrons from $MAPbI_3$.[14–20] These co-catalysts facilitate the reduction of protons present in aqueous HI solution to generate H_2. As a result, the rates of HER in $MAPbI_3$-based composites were significantly improved compared to $MAPbI_3$ alone. These findings offer valuable insights into the modulation of charge transportation for enhancing the photocatalytic performance of hybrid perovskite nanocrystals in hydrogen evolution reactions.

In recent years, several efforts were made to enhance the HER activities of $MAPbI_3$ by tagging a co-catalyst as previously discussed. However, there have been limited studies focusing on the enhancement of the hydrogen evolution rates of pristine $MAPbI_3$.[21–24] For an efficient photocatalyst, its characteristics like surface area, morphology, and particle dimensions are crucial parameters that exert a notable impact on the efficiency of the hydrogen evolution reaction (HER).[25–27] In a chemical reaction, parameters like reaction temperature, reaction time, the concentrations of reactants, and solvent polarity play a crucial role in determining the morphology of the resulting product.[28] In this study, we have investigated how the variation in solvents from polar protic to polar aprotic can alter the surface area and surface morphology. In this study, keeping the reactant concentration constant, we have fabricated $MAPbI_3$ (MAPI) using two distinct methods, wherein the variation in the solvent medium results in two different morphologies that lead to discrepancies in the efficiency of photocatalytic and photoelectrochemical processes. The cuboid morphology of MAPI was facilitated by the polar protic solvent HI, in contrast with the rodlike shape of MAPI facilitated by the polar aprotic solvent DMF. The rod-shaped MAPI produced with DMF (referred to as $MAPI_{DMF}$) exhibited superior performances in both photocatalytic and photoelectrochemical activities compared to the cuboid-shaped MAPI synthesized with HI (referred to as $MAPI_{HI}$).

To improve the performance of $MAPI_{DMF}$ in a more effective way, a polyfluorene based polymer has been incorporated with $MAPI_{DMF}$ as a co-catalyst *via in situ* fabrication. ($MAPI_{DMF}/PF_{10}$) composites were prepared with 10 wt% polyfluorene with respect to MAPI. Conjugated polymeric materials can easily absorb visible light irradiation as they possess extended and delocalized π-systems, leading to their application in organic photonics and organic electronics as well as photocatalytic hydrogen evolution. The π-conjugated polyfluorene core functions as an antenna system that efficiently channels the electrons produced by the absorbed solar radiation originating from the photo-absorber (MAPI) and subsequently transports them within the solution. 10 wt% polyfluorene integrated on the $MAPI_{DMF}$ surface ($MAPI_{DMF}/PF_{10}$) exhibited a maximum hydrogen evolution rate of 6200 μmol h^{-1} g^{-1}. The as-prepared composites were fully characterized through UV-visible spectroscopy, XRD, FESEM, Brunauer, Emmett, and Teller (BET) surface area analysis, steady state photoluminescence, three-electrode electrochemical and photoelectrochemical techniques. Among all three samples, $MAPI_{DMF}/PF_{10}$ performed the best, while $MAPI_{HI}$ exhibited the lowest values.

Results and discussion

The as-prepared $MAPI_{HI}$ and $MAPI_{DMF}$ powders were analyzed by XRD as shown in Fig. 1a. The as-prepared $MAPI_{HI}$ and $MAPI_{DMF}$ powders have indistinguishable XRD patterns with the standard ones, confirming the successful formation of a single-phase product.[18] This indicates that, even after solvent change, the perovskite crystal structure remains intact. Even after the incorporation of the polyfluorene co-catalyst, for $MAPI_{DMF}/PF_{10}$ no changes in the XRD pattern were observed. Even after 80 hours of white light irradiation inside aqueous HI solution, $MAPI_{DMF}/PF_{10}$ composites retained their crystal structure, evident from the XRD patterns (Fig. S1, ESI†).

The sunlight absorption properties within the visible range were further studied by UV-vis spectroscopy for pristine $MAPI_{HI}$, $MAPI_{DMF}$, and $MAPI_{DMF}/PF_{10}$ composites. As shown in Fig. 1b, $MAPI_{DMF}$ has a slightly higher absorbance as compared to $MAPI_{HI}$.[29] Upon addition of a polyfluorene co-catalyst, there was a noticeable enhancement in light absorption. The light absorption range was further extended up to 850 nm as well. It is notable that the elongated absorption tail plays a crucial role in improving the efficiency of solar-to-hydrogen conversion.[30]

To understand the effect of solvent on morphology in great detail, field emission SEM was employed. Pristine MAPI is highly crystalline in nature. Fig. 2a and b demonstrates the fact that drastic changes in morphology were observed by the change of the reaction medium from HI to DMF. HI assisted MAPI ($MAPI_{HI}$) showed a morphology corresponding to a cuboid structure and a smooth surface, whereas MAPI prepared in DMF reaction medium showed microrod shaped morphology. This substantial transformation in shape and morphology affects various facets of photocatalytic and photochemical performances.[31–33] Moreover, the incorporation of polyfluorene as a co-catalyst with $MAPI_{DMF}$ resulted in the formation of microstructures where small clusters of polyfluorene moieties were uniformly dispersed and firmly embedded on the surface of MAPI, indicating a strong integration between MAPI and polyfluorene (Fig. 2c). The robust heterojunction was a result of

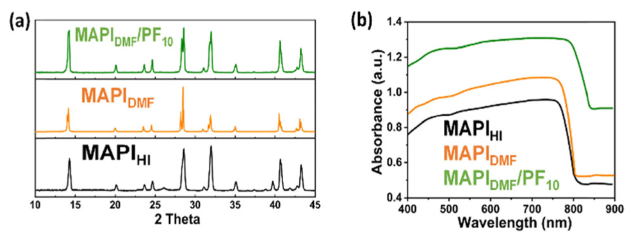

Fig. 1 (a) XRD diffractograms and (b) UV-visible spectra of pristine MAPI and composites.

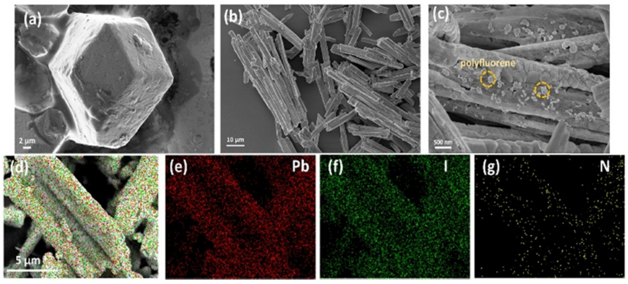

Fig. 2 FESEM images of (a) $MAPI_{HI}$, (b) $MAPI_{DMF}$, and (c) $MAPI_{DMF}/PF_{10}$. EDX elemental mapping of (d) all elements, (e) Pb, (f) I, and (g) N.

the *in situ* crystallization technique that was utilized for the synthesis. Energy dispersive X-ray spectroscopy was conducted to observe the distribution of elements on the entire MAPI surface. Elemental mapping of the $MAPI_{DMF}$/polyfluorene photocatalyst composite (Fig. 2d–g) depicts that the Pb, I and N atoms (contributed by MAPI) were observed to be uniformly distributed throughout the crystal. Transmission electron microscopy (TEM) was utilized to study the heterojunction of polyfluorene with the perovskite phase in detail. The $MAPI_{DMF}/PF_{10}$ heterocatalyst exhibited the typical rod like morphology of the perovskite phase (high density contrast due to the presence of Pb) and the granular morphology of the PF polymer (low density contrast globular shape) anchored on the perovskite microrod, similar to the SEM observation (Fig. S2, ESI†).

The rate of hydrogen evolution reaction is regulated by the specific surface area. The quantity of photons striking the photocatalyst surface is positively correlated with the activity of HER, indicating that the reaction occurs on the surface of the photocatalyst.[34–36] Fig. 3a depicts the adsorption–desorption isotherms of both $MAPI_{HI}$ and $MAPI_{DMF}$. The adsorption–desorption isotherms of both samples were of type II (BDDT classification).[37] The isotherm pertaining to $MAPI_{DMF}$ shifted towards a greater magnitude of absorbed quantity compared to $MAPI_{HI}$. The hysteresis loop for $MAPI_{DMF}$ was spread over the entire region of relative pressure, whereas for $MAPI_{HI}$ the hysteresis loop shifted towards lower relative pressure. BET analysis of the samples showed a surface area of 1.333 $m^2\ g^{-1}$ and 7.875 $m^2\ g^{-1}$ for $MAPI_{HI}$ and $MAPI_{DMF}$ microcrystals, respectively.

The average pore size of $MAPI_{HI}$ and $MAPI_{DMF}$ was evaluated as 7.115 nm and 3.421 nm, respectively, as depicted in Fig. 3b, indicating both samples were mesoporous in nature. In the case of the $MAPI_{HI}$ sample, there is also a notable expansion of the nanopores. The pore size distribution curve of the $MAPI_{DMF}$ sample exhibits a considerable breadth with the presence of an additional peak ranging from 6 nm to 11 nm as evident from visual inspection. This phenomenon suggests a higher pore abundance in $MAPI_{DMF}$, leading to a larger pore volume of 0.011 $cm^3\ g^{-1}$ in comparison to $MAPI_{HI}$ (0.002 $cm^3\ g^{-1}$). Table 1 summarizes the physical characteristics of the photocatalysts. In essence, the BET specific surface areas display a steady increase from 1.333 $m^2\ g^{-1}$ to 7.875 $m^2\ g^{-1}$ upon changing the solvent from HI to DMF, thereby directly influencing the photocatalytic and photochemical properties.

Table 1 Surface area, pore size, pore volume and HER activities of $MAPI_{HI}$ and $MAPI_{DMF}$

Sample	S_{BET} ($m^2\ g^{-1}$)	Pore size (nm)	Pore volume ($cm^3\ g^{-1}$)	HER activity (μmol $h^{-1}\ g^{-1}$)
$MAPI_{HI}$	1.333	7.115	0.002	30
$MAPI_{DMF}$	7.875	3.421	0.011	830

To explore the interplay between MAPI and the polyfluorene co-catalyst, the XPS technique was employed for $MAPI_{DMF}/PF_{10}$ composites. Fig. 4a shows the survey scan of the $MAPI_{DMF}$ sample which revealed the existence of Pb, I, N, and C elements. Specifically, the 4f Pb state of pristine $MAPI_{DMF}$ exhibited distinct peaks at 143.32 eV and 138.44 eV, corresponding to the Pb $4f_{5/2}$ and $4f_{7/2}$ states, respectively. Conversely, the I 3d state of pristine $MAPI_{DMF}$ displayed two peaks at 630.31 eV and 618.81 eV, attributed to the I $3d_{3/2}$ and I $3d_{5/2}$ states. Upon introduction of the polyfluorene co-catalyst on the $MAPI_{DMF}$ surface, a notable shift towards higher binding energies was observed for both Pb 4f and I 3d states, as illustrated in Fig. 4b and c. These findings consistently imply a synergy between MAPI and the polyfluorene co-catalyst, indicating an efficient electron transfer from $MAPI_{DMF}$ to polyfluorene.[29]

The photocatalytic activities of the as-prepared pristine $MAPI_{HI}$, $MAPI_{DMF}$ and $MAPI_{DMF}/PF_{10}$ composites were confirmed through gas chromatography under visible light where photocatalyst powders were immersed in a solution of HI and

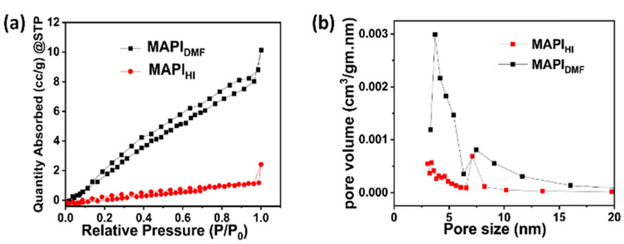

Fig. 3 (a) Surface area and (b) pore size distribution of $MAPI_{DMF}$ and $MAPI_{HI}$.

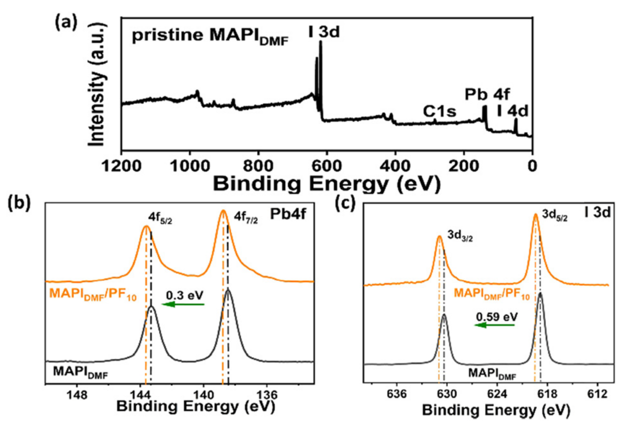

Fig. 4 (a) XPS survey scan of $MAPI_{DMF}$ and high resolution XPS of (b) Pb and (c) I.

phosphorous acid (H_3PO_2) saturated with methylammonium lead iodide (MAPI). Cube shaped HI assisted MAPI ($MAPI_{HI}$) exhibited a trace amount of H_2 evolution activity (30 μmol h^{-1} g^{-1}) owing to the lack of active photoactive reaction sites and rapid photogenerated electron recombination on the pristine $MAPI_{HI}$ surface.[16] Surprisingly, DMF assisted MAPI ($MAPI_{DMF}$) exhibited an HER activity of 830 μmol h^{-1} g^{-1}. The boosted HER activity of $MAPI_{DMF}$ upon the change of the solvent system from HI to DMF might be attributed to the larger surface area of rod shaped $MAPI_{DMF}$. As all photocatalytic reactions take place on the catalyst (MAPI) surface, a greater surface area leads to a greater number of reaction sites and a greater number of photons will be absorbed on $MAPI_{DMF}$ surfaces, owing to the almost 28 times higher HER activity of $MAPI_{DMF}$.

To further enhance the performance of the photocatalyst, the polyfluorene co-catalyst (10 wt%) was integrated on the $MAPI_{DMF}$ surface. $MAPI_{DMF}$/polyfluorene composites were prepared by *in situ* fabrication which creates an intimate heterojunction between $MAPI_{DMF}$ and polyfluorene co-catalyst particles. The hydrogen evolution rates for all the samples were compiled and are presented as a function of the duration of light exposure in Fig. 5a. The hydrogen evolution reaction activity for HI splitting was significantly boosted upon incorporation of co-catalysts. While $MAPI_{DMF}$ exhibited an HER activity of 830 μmol h^{-1} g^{-1}, $MAPI_{DMF}/PF_{10}$ composites exhibited a maximum HER rate of 6200 μmol h^{-1} g^{-1}. After loading of 10 wt% polyfluorene on $MAPI_{DMF}$, hydrogen evolution rates accelerated 7 times from the previous one. Further increment in co-catalyst loading percentage did not affect the photocatalytic activity.

It is worth mentioning that *in situ* fabrication also facilitated the enhanced photocatalytic activity of $MAPI_{DMF}/PF_{10}$ composites. In this process, the co-catalysts were deeply embedded on MAPI surfaces. Such intimate integration forms a strong heterojunction which decreases the likelihood of MAPI and polyfluorene separation under magnetic stirring during HER activity. The $MAPI_{DMF}$/polyfluorene composites not only exhibited superior performances to pristine MAPI, they also outperformed Pt deposited MAPI in terms of HER activity.[38] In terms of photocatalytic stability, $MAPI_{DMF}$/polyfluorene composites exhibited stability for a prolonged time period. Photocatalytic hydrogen evolution reactions were performed for $MAPI_{DMF}/PF_{10}$ for 80 hours under visible light irradiation as depicted in Fig. 5b. No considerable changes in the hydrogen evolution rate were observed for 56 hours. Polyfluorene, due to its long hydrophobic moiety, protects MAPI from structural degradation in the water environment. In the last 3 cycles, a significant decline in the H_2 evolution rate was observed, which might be due to depletion of H_3PO_2. This depletion hinders the I_3^- to I^- conversion, resulting in excess generation of I_3^- ions that could inhibit the absorption of light by the MAPI composites also hindering efficient hole extraction.[39]

The intensity of photoluminescence strongly correlates with electron–hole radiative recombination. A higher photoluminescence intensity indicates a greater extent of radiative recombination and consequently a lower degree of charge separation and reduced photocatalytic activity. As depicted in Fig. 6a, all samples exhibited photoluminescence emission at around 759 nm with different intensities owing to their varied degree of radiative charge recombination. It is worth mentioning that MAPI synthesized in two different solvents displayed distinct PL intensities of dissimilar manners. Notably, $MAPI_{HI}$ demonstrated the highest photoluminescence intensity, whereas $MAPI_{DMF}$ showed significantly lower levels. The enlargement of the surface area of a photocatalyst can directly influence the rate of electron–hole recombination within the material. As indicated by the BET surface area analysis, the surface area of $MAPI_{DMF}$ is 7 times greater than that of $MAPI_{HI}$. This increased surface area of $MAPI_{DMF}$ may result in a lower likelihood of radiative charge recombination, leading to improved charge separation and enhanced photocatalytic performance.[40] To further enhance the efficiency of $MAPI_{DMF}$, heterostructures of MAPI/polyfluorene ($MAPI_{DMF}/PF_{10}$) were fabricated with 10 weight percent of polyfluorene on the surfaces of $MAPI_{DMF}$. Among all the photocatalysts, $MAPI_{DMF}/PF_{10}$ exhibited the lowest PL intensity, indicating the most efficient charge separation and alternate charge migration pathway different from radiative recombination.

To explore the role of the polyfluorene co-catalyst embedded on the $MAPI_{DMF}$ surface, we performed a series of photoelectrochemical measurements. The photoelectrochemical (PEC)

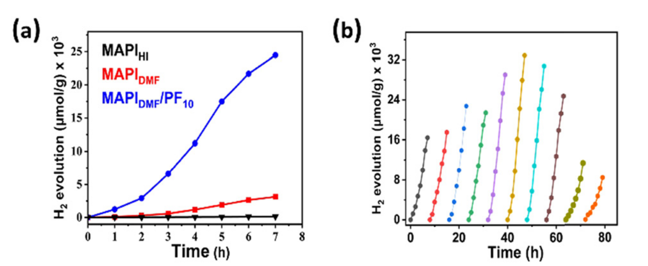

Fig. 5 (a) Comparative HER activities of all samples. (b) 80 hour long stability study of $MAPI_{DMF}/PF_{10}$.

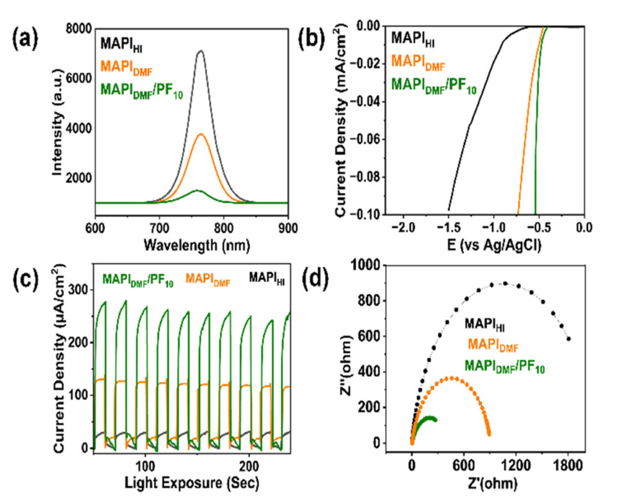

Fig. 6 (a) Steady state PL, (b) polarization curves, (c) transient photocurrent, and (d) EIS Nyquist plots of $MAPI_{HI}$, $MAPI_{DMF}$ and $MAPI_{DMF}/PF_{10}$.

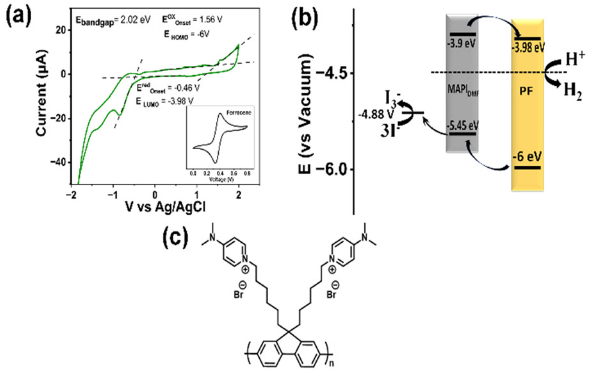

Fig. 7 (a) CV curve of PF. (b) Energy band diagram. (c) Molecular structure of the polyfluorene (PF) polymer.

analysis is commonly utilized to provide compelling evidence for the charge separation and transfer in the photocatalyst composites.

Fig. 6b presents the cathodic polarization curves (*I–V* curves) of pristine $MAPI_{HI}$, $MAPI_{DMF}$ and $MAPI_{DMF}/PF_{10}$. These results indicate the occurrence of the hydrogen evolution reaction for all the catalysts. Furthermore, the $MAPI_{DMF}/PF_{10}$ composites showed a smaller overpotential compared to $MAPI_{HI}$ and $MAPI_{DMF}$, which suggested that polyfluorene could reduce the overpotential resulting in more favourable electrocatalytic HER kinetics of $MAPI_{DMF}/PF_{10}$. This observation explains the accelerated rate of photocatalytic reductive hydrogen evolution reaction. This may be due to polyfluorene, which provides better charge separation and charge transport for photocatalysis.[41]

The photo-current responses for the pristine $MAPI_{HI}$, pristine $MAPI_{DMF}$, $MAPI_{DMF}/PF_{10}$ under several 10 s on/off illumination windows were measured and are presented in Fig. 6c. Unambiguously, in the case of turn-on conditions, the photocurrent intensity was observed to remain almost unchanged and promptly reduced to zero when the light was turned off, signifying a swift photocurrent response to light on–off conditions. $MAPI_{DMF}$ exhibited a higher photocurrent compared to $MAPI_{HI}$, while $MAPI_{HI}$ had the lowest value as expected. $MAPI_{DMF}/PF_{10}$ heterostructures exhibited the highest photocurrent under the same electric bias. In terms of transient photocurrent, a higher value indicates the occurrence of efficient charge migration in $MAPI_{DMF}/PF_{10}$ composites.[42,43] These results were well validated by electrochemical impedance spectroscopy (EIS) measurement as shown in Fig. 6d, and $MAPI_{DMF}/PF_{10}$ with the smallest semicircle arc dictates the lowest interfacial charge transfer resistance resulting in expedited interfacial charge transfer.[39] For pristine MAPI, the interfacial charge transfer resistance gradually increases and it is maximum for pristine $MAPI_{HI}$.

To investigate the electron transfer pathway in the $MAPI_{DMF}/PF_{10}$ composite, an initial investigation was conducted on MAPI using ultraviolet photoelectron spectroscopy (UPS) analysis. The valance band maximum of $MAPI_{DMF}$ was determined to be −5.45 eV from UPS, while the bandgap was calculated to be 1.55 eV using the Tauc plot. The conduction band minimum was estimated as −3.9 eV (Fig. S3 and S4, ESI†). In order to determine the HOMO and LUMO of polyfluorene, the cyclic voltammetry experiment was carried out, which revealed the values of E^{red}_{onset} and E^{OX}_{onset} were −0.46 V and 1.56 V for the polyfluorene co-catalyst as shown in Fig. 7a. Subsequently, the HOMO and LUMO of polyfluorene were determined as −3.98 eV and 6 eV.[44,45] The optical bandgap was calculated as 2.02 eV.

Regarding the band structure of the overall composite, a type II heterojunction at the interface of polyfluorene and $MAPI_{DMF}$ was proposed, as illustrated in Fig. 7b, showcasing an ideal scenario for the photocatalytic HER process. For H_2 evolution according to "band matching" theory, the CBM energy level of $MAPI_{DMF}$ was found to be more positive than that of polyfluorene, enabling the migration of photo-generated electrons from MAPI to polyfluorene. This phenomenon accelerates effective extraction of the photogenerated electrons for the reduction of protons in the reaction medium to generate H_2. Consequently, the photoexcitons can be effectively separated, leading to a significant enhancement in the photocatalytic HER activity of the $MAPI_{DMF}/PF_{10}$ heterostructures.[46,47]

Conclusions

The role of solvent assisted morphology dependent MAPI has been investigated for photocatalytic and photoelectrochemical activities. This article summarizes the fact that the change of the reaction medium from HI to DMF not only alters the surface morphology from the cuboid to rod shape, and it also influences various aspects of photocatalytic and photoelectrochemical activities. $MAPI_{DMF}$ exhibited superior performances in terms of HER activity which was 28 times better compared to $MAPI_{HI}$. The superior HER performances of $MAPI_{DMF}$ were supported by the quenched photoluminescence intensity, higher photocurrent, and lower charge transfer resistance. The improved photocatalytic and photoelectrochemical activities might be attributed to the larger surface area of rod shaped $MAPI_{DMF}$. A greater surface area provides more reaction sites, enabling the absorption of a higher number of photons resulting in accelerated H_2 evolution. A stable $MAPbI_3$/polyfluorene composite was successfully prepared by *in situ* fabrication. The incorporation of polyfluorene on $MAPI_{DMF}$ surfaces not only broadens the light absorption range but also enhances charge segregation and transport at the $MAPI_{DMF}/PF_{10}$ interface, leading to improved photocatalytic and photoelectrochemical activities. Under optimized conditions, $MAPI_{DMF}/PF_{10}$ exhibited a maximum HER activity of 6200 μmol h^{-1} g^{-1}. The enhanced HER activity of $MAPI_{DMF}/PF_{10}$ may be attributed to the efficient interfacial charge transfer from $MAPI_{DMF}$ to the polyfluorene co-catalyst owing to proper alignment of the CBM of $MAPI_{DMF}$ and the LUMO of polyfluorene. This work shows the immense possibilities of utilizing rationally designed metal free organic conjugated polymers for semiconductor photocatalysis applications, provided the physicochemical stability and band alignment criteria are well met.

Abbreviations

CBM	Conduction band minima
MAPI	Methylammonium lead iodide
PF	Poly(fluorene)
PL	Photoluminescence

Author contributions

Tamal Pal: conceptualization, methodology, validation, formal analysis, investigation, data curation, writing – original draft, visualization. Soumalya Bhowmik: validation, investigation, writing – review & editing, visualization. Arvin Sain Tanwar: methodology, resources. Ameer Suhail: resources, data curation. Nageswara Rao Peela: resources. Chivukula V. Sastri: supervision, project administration. Parameswar Krishnan Iyer: supervision, project administration, funding acquisition.

Data availability

The data supporting this article have been included as part of the ESI.†

Conflicts of interest

The authors declare no conflicts of interest.

Acknowledgements

P. K. I. acknowledges the financial grants from DST, India, through the projects DST/TSG/PT/2009/23, DST/TMD/IC-MAP/2K20/03 and DST/CRG/2019/002164, Deity, India, no. 5(9)/2012-NANO (Vol. II), Max-Planck-Gesellschaft IGSTC/MPG/PG(PKI)/2011A/48 and SPARC project SPARC/2018-2019/P1097/SL. N. R. P. acknowledges the financial support from DST SERB, New Delhi, India under a core research grant (CRG, File No. CRG/2022/005144). C. V. S. acknowledges the financial support from DST SERB, New Delhi, India through the grant code CRG/2023/000456. T. P., A. S. N. and A. S. M. are thankful to the Ministry of Education, Govt. of India for financial support. S. B. acknowledges the financial grants and fellowship from PMRF, Ministry of Education, India (grant no. 1900823). The Department of Chemistry, Centre for Nanotechnology and CIF IIT Guwahati are acknowledged for instrument facilities. We express special gratitude to Dr. Mohammad Adil Afroz (IIT Roorkee, India) for assistance in XPS and UPS study.

References

1 C. Dai and B. Liu, *Energy Environ. Sci.*, 2020, **13**, 24–52.
2 C. J. Quarton, O. Tlili, L. Welder, C. Mansilla, H. Blanco, H. Heinrichs, J. Leaver, N. J. Samsatli, P. Lucchese, M. Robinius and S. Samsatli, *Sustainable Energy Fuels*, 2020, **4**, 80–95.
3 H. Tong, S. Ouyang, Y. Bi, N. Umezawa, M. Oshikiri and J. Ye, *Adv. Mater.*, 2012, **24**, 229–251.
4 A. Kudo and Y. Miseki, *Chem. Soc. Rev.*, 2009, **38**, 253–278.
5 A. A. Ismail and D. W. Bahnemann, *Sol. Energy Mater. Sol. Cells*, 2014, **128**, 85–101.
6 J. Burschka, N. Pellet, S.-J. Moon, R. Humphry-Baker, P. Gao, M. K. Nazeeruddin and M. Grätzel, *Nature*, 2013, **499**, 316–319.
7 C. Eames, J. M. Frost, P. R. F. Barnes, B. C. O'Regan, A. Walsh and M. S. Islam, *Nat. Commun.*, 2015, **6**, 1–8.
8 G. Xing, N. Mathews, S. Sun, S. S. Lim, Y. M. Lam, M. Grätzel, S. Mhaisalkar and T. C. Sum, *Science*, 2013, **342**, 344–347.
9 R. Garai, R. K. Gupta, M. Hossain and P. K. Iyer, *J. Mater. Chem. A*, 2021, **9**, 26069–26076.
10 A. Kojima, K. Teshima, Y. Shirai and T. Miyasaka, *J. Am. Chem. Soc.*, 2009, **131**, 6050–6051.
11 R. Garai, M. A. Afroz, R. K. Gupta and P. K. Iyer, *Adv. Sustainable Syst.*, 2020, **4**, 202000078.
12 R. Garai, R. K. Gupta, A. S. Tanwar, M. Hossain and P. K. Iyer, *Chem. Mater.*, 2021, **33**, 5709–5717.
13 S. Park, W. J. Chang, C. W. Lee, S. Park, H.-Y. Ahn and K. T. Nam, *Nat. Energy*, 2016, **2**, 1–8.
14 W. Han, Y. Wei, J. Wan, N. Nakagawa and D. Wang, *Inorg. Chem.*, 2022, **61**, 5397–5404.
15 W. Guan, Y. Li, Q. Zhong, H. Liu, J. Chen, H. Hu, K. Lv, J. Gong, Y. Xu, Z. Kang, M. Cao and Q. Zhang, *Nano Lett.*, 2021, **21**, 597–604.
16 C. Cai, Y. Teng, J.-H. Wu, J.-Y. Li, H.-Y. Chen, J.-H. Chen and D.-B. Kuang, *Adv. Funct. Mater.*, 2020, **30**(35), 2001478, DOI: 10.1002/adfm.202001478.
17 Y. Zhao, Q. Zeng, Y. Yu, T. Feng, Y. Zhao, Z. Wang, Y. Li, C. Liu, J. Liu, H. Wei, S. Zhu, Z. Kang, H. Zhang and B. Yang, *Mater. Horiz.*, 2020, **7**, 2719–2725.
18 R. Li, X. Li, J. Wu, X. Lv, Y.-Z. Zheng, Z. Zhao, X. Ding, X. Tao and J.-F. Chen, *Appl. Catal., B*, 2019, **259**, 118075.
19 L. Jiang, Y. Guo, S. Qi, K. Zhang, J. Chen, Y. Lou and Y. Zhao, *Dalton Trans.*, 2021, **50**, 17960–17966.
20 Y. Wu, P. Wang, X. Zhu, Q. Zhang, Z. Wang, Y. Liu, G. Zou, Y. Dai, M.-H. Whangbo and B. Huang, *Adv. Mater.*, 2018, **30**(7), 1704342, DOI: 10.1002/adma.201704342.
21 Q. Yao, H. Li, J. Xue, S. Jiang, Q. Zhang and J. Bao, *Angew. Chem., Int. Ed.*, 2023, **62**, e202308140, DOI: 10.1002/anie.202308140.
22 J. Liu, H. Zhang, J. Wang and X. Zong, *J. Mater. Chem. A*, 2024, **12**, 5740–5747.
23 H. Fu, X. Liu, J. Fu, Y. Wu, Q. Zhang, Z. Wang, Y. Liu, Z. Zheng, H. Cheng, Y. Dai, B. Huang and P. Wang, *ACS Catal.*, 2023, **13**, 14716–14724.
24 T. Sheikh, S. Maqbool, P. Mandal and A. Nag, *Angew. Chem., Int. Ed.*, 2021, **60**, 18265–18271.
25 J. Yu, Y. Yu, P. Zhou, W. Xiao and B. Cheng, *Appl. Catal., B*, 2014, **156–157**, 184–191.
26 Z. Liu, Y. Zhuang, L. Dong, H. Mu, D. Li, F. Zhang, H. Xu and H. Xie, *ACS Appl. Energy Mater.*, 2023, **6**, 7722–7736.

27 F. Vaquero, R. M. Navarro and J. L. G. Fierro, *Appl. Catal., B*, 2017, **203**, 753–767.
28 Z. Jin, T. Li, L. Zhang, X. Wang, G. Wang and X. Hao, *J. Mater. Chem. A*, 2022, **10**, 1976–1991.
29 J. Yu and X. Xu, *Energy Mater. Adv.*, 2022, **2022**, 5464258.
30 Yukta, N. Parikh, R. D. Chavan, P. Yadav, M. K. Nazeeruddin and S. Satapathi, *ACS Appl. Mater. Interfaces*, 2022, **14**, 29744–29753.
31 Z. Wang, K. Lv, G. Wang, K. Deng and D. Tang, *Appl. Catal., B*, 2010, **100**, 378–385.
32 M. Wang, G. Zhang, Z. Guan, J. Yang and Q. Li, *Small*, 2021, **17**, 2006952, DOI: 10.1002/smll.202006952.
33 S. Cao, J. Jiang, B. Zhu and J. Yu, *Phys. Chem. Chem. Phys.*, 2016, **18**, 19457–19463.
34 P. Chen, L. Chen, S. Ge, W. Zhang, M. Wu, P. Xing, T. B. Rotamond, H. Lin, Y. Wu and Y. He, *Int. J. Hydrogen Energy*, 2020, **45**, 14354–14367.
35 S. Sun, H. Li and Z. J. Xu, *Joule*, 2018, **2**, 1024–1027.
36 D. Feng, Y. Cheng, J. He, L. Zheng, D. Shao, W. Wang, W. Wang, F. Lu, H. Dong, H. Liu, R. Zheng and H. Liu, *Carbon*, 2017, **125**, 454–463.
37 L. Camacho-Escobar, R. E. Palma-Goyes, J. Ortiz-Landeros, I. Romero-Ibarra, O. A. Gamba-Vásquez and J. Vazquez-Arenas, *Appl. Surf. Sci.*, 2020, **521**, 146357.
38 X. Zhao, S. Chen, H. Yin, S. Jiang, K. Zhao, J. Kang, P. F. Liu, L. Jiang, Z. Zhu, D. Cui, P. Liu, X. Han, H. G. Yang and H. Zhao, *Matter*, 2020, **3**, 935–949.
39 F. Wang, X. Liu, Z. Zhang and S. Min, *Chem. Commun.*, 2020, **56**, 3281–3284.
40 R.-K. Ye, S.-S. Sun, L.-Q. He, S.-R. Yang, X.-Q. Liu, M.-D. Li, P.-P. Fang and J.-Q. Hu, *Appl. Catal., B*, 2021, **291**, 120107.
41 Q. Liu, J. Shi, J. Hu, A. M. Asiri, Y. Luo and X. Sun, *ACS Appl. Mater. Interfaces*, 2015, **7**, 3877–3881.
42 M. Zhu, M. Fujitsuka, L. Zeng, M. Liu and T. Majima, *Appl. Catal., B*, 2019, **256**, 117864.
43 X. Liu, Q. Zhang, S. Zhao, Z. Wang, Y. Liu, Z. Zheng, H. Cheng, Y. Dai, B. Huang and P. Wang, *Adv. Mater.*, 2023, **35**, e2208915, DOI: 10.1002/adma.202208915.
44 P. Gopikrishna, D. Das, L. R. Adil and P. K. Iyer, *J. Phys. Chem. C*, 2017, **121**, 18137–18143.
45 W. Wu, C. Dai, Y. Deng, Y. Chen, F. Li and C. Zeng, *Adv. Energy Sustainable Res.*, 2022, **3**(10), 2200068, DOI: 10.1002/aesr.202200068.
46 T. Liu, S. Zhou, J. Qi, K. Wang, L. Zheng, Q. Huang, T. Zhou and J. Zhang, *J. Energy Chem.*, 2021, **58**, 370–376.
47 H. Yang, D. Ma, Y. Li, Q. Zhao, F. Pan, S. Zheng and Z. Lou, *Chin. J. Struct. Chem.*, 2023, **42**, 100031.